

## Extremely large magnetoresistance, anisotropic Hall effect, and Fermi surface topology in single-crystalline WSi<sub>2</sub>

Rajib Mondal <sup>1,\*</sup> Souvik Sasmal <sup>1</sup> Ruta Kulkarni,<sup>1</sup> Arvind Maurya,<sup>2</sup> Ai Nakamura,<sup>2</sup> Dai Aoki,<sup>2</sup> Hisatomo Harima <sup>3</sup> and Arumugam Thamizhavel <sup>1,†</sup>

<sup>1</sup>*Department of Condensed Matter Physics and Materials Science, Tata Institute of Fundamental Research, Homi Bhabha Road, Colaba, Mumbai 400 005, India*

<sup>2</sup>*Institute for Materials Research, Tohoku University, Oarai, Ibaraki 311-1313, Japan*

<sup>3</sup>*Department of Physics, Graduate School of Science, Kobe University, Kobe 657-8501, Japan*



(Received 27 May 2020; accepted 9 September 2020; published 28 September 2020)

We report on the observation of a nonsaturating, extremely large magnetoresistance (XMR) and the Fermi surface topology of a high quality WSi<sub>2</sub> single crystal grown by the Czochralski method. The magnetoresistance at  $T = 2$  K reaches a value  $\approx 10^5\%$  in 14 T magnetic field with no sign of saturation. The Hall resistivity data of WSi<sub>2</sub> was found to be highly anisotropic. The analysis of magnetoconductivity data of WSi<sub>2</sub> revealed a near compensation of charge carrier with relatively low carrier density as compared to that of a normal metal. The observed anisotropic Hall resistivity in WSi<sub>2</sub> is due to the presence of multiple bands and Fermi pockets responsible for the transport phenomena in it. The extremely large carrier mobility and near compensation of charge carriers are responsible for the nonsaturating XMR behavior in WSi<sub>2</sub> crystal. The band structure calculation and de Haas-van Alphen effect measurement depict a cylindrical Fermi surface from which the associated quantum parameters have been obtained. The magnetotransport data of WSi<sub>2</sub> along both the crystallographic directions follows the universal temperature-field triangular phase diagram as observed in other materials exhibiting XMR behavior.

DOI: [10.1103/PhysRevB.102.115158](https://doi.org/10.1103/PhysRevB.102.115158)

### I. INTRODUCTION

Of late, there is a tremendous research interest in condensed matter physics towards materials that possess novel quantum states and has a direct correspondence with the elementary particle in high energy physics. The elementary quasiparticles, like Dirac, Weyl, and Majorana fermions that have been the subject of discussion for long in high energy physics are now uncovered and observed experimentally in crystals with various topologically protected surface state properties [1–11]. These topological phases exhibit physical properties like extremely large magnetoresistance (XMR) and other interesting magnetotransport phenomena such as topologically nontrivial Berry phase in quantum oscillations [12–19] etc. Elemental Bi, being a prototype semimetal, exhibits a huge nonsaturating magnetoresistance (MR) [20]. It is well documented in literature that the extremely large carrier mobility, large mean free path of electron, and the compensation of charge carrier lead to such XMR phenomena in nonmagnetic (diamagnetic) semimetals [4,12–19,21,22]. Recently, many such nonmagnetic (diamagnetic) semimetals have been discovered whose MR was found to be as large as  $\approx 10^5\%$ . Depending on the band struc-

ture near the Fermi level and the Fermi surface topology in the compounds, semimetals can be classified into several categories. Dirac, Weyl, and compensated semimetals are of special interest to the researchers in current times due to their exotic electrical and magnetotransport properties. To name a few, the materials exhibiting such XMR behavior are MoTe<sub>2</sub>, WTe<sub>2</sub>, NbP, NbAs, LaSb, YSb, LaBi, TaP, TaAs, MoP<sub>2</sub>, WP<sub>2</sub> etc. [7,11–14,16–18,21–24]. The electron-hole compensation and the large carrier mobility ( $\approx 10^4$  cm<sup>2</sup>/V s) with relatively less carrier concentration ( $\approx 10^{19}$  cm<sup>-3</sup>) in those semimetals leads to such XMR behavior [12,13,18,22]. From the application point of view, the phenomena of topologically protected surface states which lead to various interesting physical and magnetotransport behavior can be of potential applications in spintronic devices, low-power electronic devices, and also for the advancement in qubits [25].

In the quest for new materials exhibiting such phenomena, recently we reported the magnetotransport properties of MoSi<sub>2</sub> single crystal which crystallizes in the tetragonal crystal structure with space group  $I4/mmm$  [26]. The magnetoresistance of MoSi<sub>2</sub> attains a value  $\approx 10^7\%$  in an applied field of 14 T for  $J \parallel [100]$  and  $H \parallel [001]$  which is comparable to the value obtained for WTe<sub>2</sub> and other topological semimetals discovered in recent times [7,11–14,17,18,21,22,26,27]. In continuation to our studies on materials exhibiting large magnetoresistance, we have successfully grown a single crystal of WSi<sub>2</sub> with an identical structure to MoSi<sub>2</sub> and present the magnetotransport and Fermi surface properties.

\*Corresponding author: mondal.rajib1988@gmail.com; Present address: UGC-DAE Consortium for Scientific Research, Kolkata Centre, Bidhannagar, Kolkata 700 106, India.

†Corresponding author: thamizh@tiffr.res.in

## II. EXPERIMENTAL DETAILS

A single crystal of  $\text{WSi}_2$  was grown by Czochralski crystal pulling method from a stoichiometric melt of high pure elements of W (99.99%, Alfa Aesar) and Si (99.999%, Alfa Aesar) using a tetra-arc furnace (Model: Techno Search, Japan). A stoichiometric quantity of W and Si with little excess amount (about 5%) of Si has been melted in a tetra-arc furnace repeatedly by flipping the ingot upside down before each melt for ensuring better homogeneity. A polycrystalline seed was cut from that ingot to grow the single crystal of  $\text{WSi}_2$ . The seed was carefully attached to the homogeneous melt of  $\text{WSi}_2$  and initially pulled at a speed of about 25 to 40 mm/h to make a necking process. Once the stable condition was achieved, the crystal was pulled at a rate of 10 mm/h for about 5 h. We obtained a single-crystalline rod of  $\text{WSi}_2$  with diameter  $\approx 4$  mm and length  $\approx 60$  mm. Energy dispersive analysis by x rays (EDAX) was performed to check the stoichiometry. A small portion of the crystal was crushed to fine powders and subjected to room temperature powder x-ray diffraction (XRD) experiment in PANalytical x-ray diffractometer equipped with a monochromatic  $\text{Cu-K}\alpha$  as the source of x rays ( $\lambda = 1.5406 \text{ \AA}$ ). Single crystalline nature of the pulled ingot was verified using x-ray Laue diffractometer. Then the crystal was oriented along the two principal crystallographic directions and cut using a spark erosion wire electric discharge machine (EDM). Electrical and magnetotransport properties were measured in the temperature range of 2–300 K in magnetic fields up to 14 T using a physical property measurement system (PPMS, Quantum Design, USA). The de Haas-van Alphen (dHvA) experiments at a constant temperature of  $\approx 35$  mK in magnetic fields up to 14.7 T using a field modulation method were carried out in a top-loading dilution refrigerator. Electronic band structure calculation and the topology of the Fermi surface of  $\text{WSi}_2$  were theoretically calculated with the input from crystallographic information using the full potential linear augmented plane wave (FLAPW) method with local density approximation (LDA) for the exchange correlation.

## III. EXPERIMENTAL RESULTS AND DISCUSSION

### A. X-ray diffraction

The room temperature powder XRD data confirmed the phase purity of  $\text{WSi}_2$  single crystal which crystallizes in a tetragonal crystal structure with space group  $I4/mmm$  (No. 139,  $D_{4h}^{17}$ ) as shown in Fig. 1(a). The lattice parameters obtained from the Rietveld refinement analysis of the powder x-ray diffraction data are  $a = 3.212(1) \text{ \AA}$  and  $c = 7.828(2) \text{ \AA}$ . The refined positional parameters of the W and Si atom are (0,0,0) and (0,0, 0.3381), occupying the  $2a$  and  $4e$  sites, respectively. EDAX analyses confirmed the nominal composition of  $\text{WSi}_2$ . The presence of distinct and well defined circular Laue diffraction spots with four fold symmetry patterns in Figs. 1(c) and 1(d) confirms the good crystalline quality.

### B. Electrical resistivity and magnetoresistivity

The temperature dependence of electrical resistivity in the range 2–300 K for current along the two principal

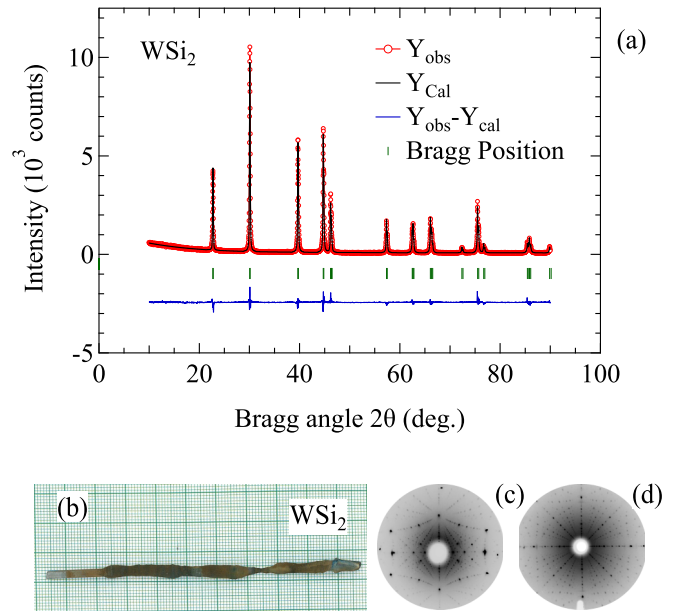


FIG. 1. (a) Room temperature powder x-ray diffraction and structural refinement by Rietveld method of  $\text{WSi}_2$ , (b) the as grown ingot, (c) back reflection Laue diffraction pattern of the (100) plane, and (d) the (001) plane.

crystallographic directions depicts metallic behavior for zero field as shown in Figs. 2(a) and 2(b). It is to be mentioned here that the anisotropy in the electrical resistivity along the two principal crystallographic directions namely [100] and [001] directions is very small. A similar behavior has been reported by Nava *et al.* [28]. The linear resistivity of  $\text{WSi}_2$  single crystal goes down steeply with lowering the temperature from 300 K to 2 K, thus resulting in a very low residual resistivity along both the directions. The residual resistivity ratio (RRR)

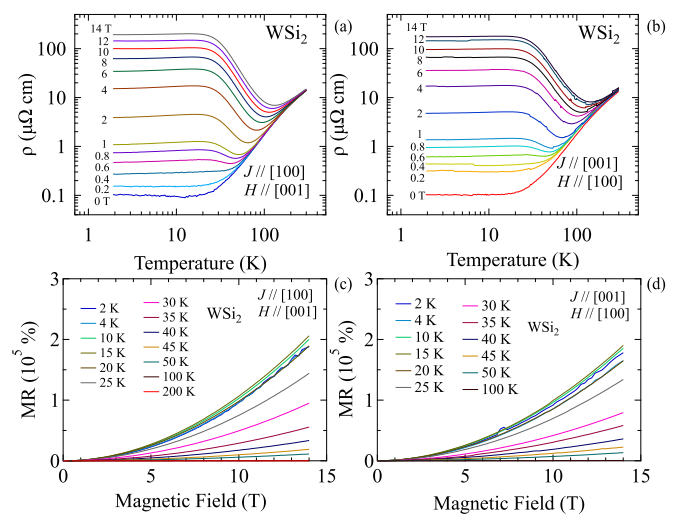


FIG. 2. (a),(b) Temperature dependence of electrical resistivity of  $\text{WSi}_2$  in zero field and different transverse magnetic fields when a field is applied along two principal crystallographic directions. (c),(d) Field dependence of transverse magnetoresistance (MR) of  $\text{WSi}_2$  at different temperatures when a field is applied along [001] and [100] directions, respectively.

was estimated as  $\approx 136$  which attests to a high quality of the grown  $\text{WSi}_2$  single crystal. The significant enhancement of transport lifetime associated with the charge carrier leads to such steep decrements of resistivity with lowering temperature which further results in a low residual resistivity  $\approx 0.103 \mu\Omega \text{ cm}$ . Such a low residual resistivity gives a signature of high transport mobility as well as high quantum mobility. The resistivity attains a value of  $\approx 14 \mu\Omega \text{ cm}$  at room temperature. Such a low resistivity in  $\text{WSi}_2$  at room temperature is even one order lower than that of the recently reported Dirac and Weyl semimetals,  $\text{Cd}_3\text{As}_2$ ,  $\text{WTe}_2$ , and  $\text{LaBi}$  etc. The observed RRR in  $\text{WSi}_2$  is comparable to that of the other topological semimetallic compounds reported in recent times [2,22,29].

In order to shed further light into the nature of low temperature resistivity in  $\text{WSi}_2$ , we have fitted the zero field resistivity data in the temperature range from 2 K to 30 K to the equation:  $\rho = \rho_0 + AT^n$ . From the fit we obtained the value of  $n$  as  $\approx 4$ , thereby indicating a deviation from the scattering mechanism dominated by electron-electron correlation ( $n = 2$ ). It is to be noted that such a deviation from pure electron-electron correlation dominated scattering mechanism has already been established in some unconventional semimetals, e.g.,  $\text{LaBi}$  ( $n = 3$ ),  $\text{LaSb}$  ( $n = 4$ ),  $\text{ZrSiS}$  ( $n = 3$ ),  $\text{WP}_2$  etc. Such a deviation could be attributed to the interband electron-phonon scattering mechanism [18,22,30].

The temperature variation of electrical resistivity of  $\text{WSi}_2$  crystal in transverse magnetic fields when current is passed along the two principal crystallographic directions is shown in Figs. 2(a) and 2(b). With the application of magnetic field, the resistivity decreases with decreasing temperature to a minimum at  $T_{\text{min}}$  from where the resistivity starts increasing until an inflection point at temperature denoted by  $T_{\text{in}}$  at which point the resistivity saturates to form a plateau. Such an increment in resistivity with field gives rise to a positive magnetoresistance in  $\text{WSi}_2$  for both the crystallographic directions. A positive MR is reminiscent to a normal metal when applied magnetic field is transverse to the driven current due the Lorentz force of the electrons. In  $\text{WSi}_2$ , we observe an extremely large magnetoresistance at low temperature upon application of high magnetic fields of 14 T as shown in Figs. 2(c) and 2(d). The transverse MR at 2 K attains a value  $\approx 2.1 \times 10^5\%$  and  $\approx 1.9 \times 10^5\%$  for  $J \parallel [100]$  and  $J \parallel [001]$ , respectively, in 14 T. Such an XMR in  $\text{WSi}_2$  is comparable to the observed XMR values in Dirac, Weyl, and compensated semimetals reported in the literature [4,7,11–14,16–18,21–23,26]. However, the observed XMR is lower than that of the isostructural  $\text{MoSi}_2$ , where a very low residual resistivity resulted in such an exotic XMR. Improved RRR in  $\text{WSi}_2$  might result in similar XMR behavior as in  $\text{MoSi}_2$ . It was also observed that there is quite strong anisotropic magnetoresistance in  $\text{MoSi}_2$  unlike in the case of  $\text{WSi}_2$  wherein a subtle anisotropic magnetoresistance has been observed which is another featuring difference in magnetoresistance behavior observed between  $\text{MoSi}_2$  and  $\text{WSi}_2$  [26]. The resistivity at low temperatures and low applied fields in those single crystals makes them potential candidates for magnetic sensors and magnetic switches.

The drastic enhancement in electrical resistivity with lowering temperature below  $T_{\text{min}}$  upon application of magnetic

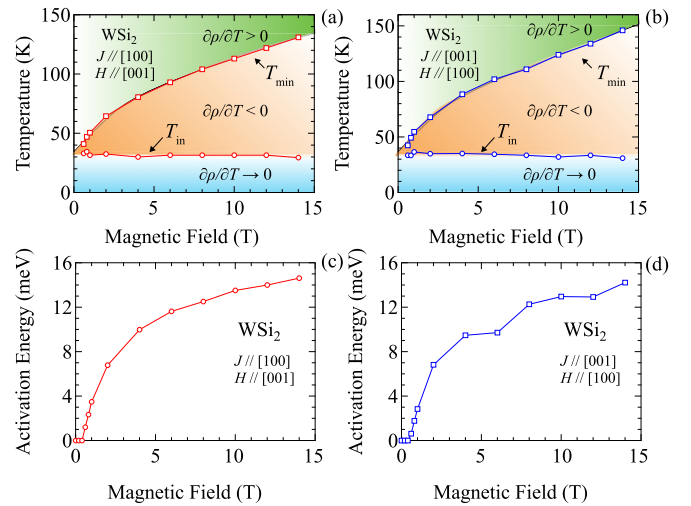


FIG. 3. (a),(b) Temperature vs magnetic field triangular phase diagram of  $\text{WSi}_2$  in various transverse applied magnetic fields when a field is applied along two principal crystallographic directions. (c),(d) Field dependence of activation energy of  $\text{WSi}_2$  when a magnetic field is applied along [001] and [100] directions, respectively.

fields in such semimetals reflects a metal to semiconductor like crossover which is even evident at low applied magnetic field of 1 T. The electrical resistivity of  $\text{WSi}_2$  also exhibits such metal-semiconductor-like crossover upon application of magnetic field which is often said to occur in topological semimetals, for example,  $\text{LaBi}$ ,  $\text{LaSb}$  owing to the opening up of a small gap at the band touching points under applied magnetic fields [22]. However, this resistivity upturn in a topological semimetal  $\text{WTe}_2$  below  $T_{\text{min}}$  is said to occur due to a strong field induced scattering [18,22,30,31].

Figures 3(a) and 3(b) show a temperature versus magnetic field phase diagram that has been constructed by calculating  $T_{\text{min}}$  and  $T_{\text{in}}$  from the plots of  $\partial\rho/\partial T$  versus  $T$  (which is not shown here for brevity). The temperature  $T_{\text{min}}$  denotes the point where  $\partial\rho/\partial T$  changes the sign upon application of magnetic field whereas  $T_{\text{in}}$  denotes the point where temperature dependent resistivity shows a maximum slope change below  $T_{\text{min}}$ , where  $\partial\rho/\partial T$  versus  $T$  shows a minimum. Upon application of magnetic field,  $T_{\text{min}}$  changes substantially, whereas  $T_{\text{in}}$  remains almost unaltered giving rise to a triangular phase diagram of temperature versus magnetic field which is reminiscent for a topological semimetal. In the narrow temperature regime between  $T_{\text{min}}$  and  $T_{\text{in}}$ , the temperature variation of resistivity of  $\text{WSi}_2$  could be fitted to the Arrhenius equation:  $\rho(T) = \rho_0 \exp(E_a/k_B T)$ , where  $E_a$  represents the activation energy of the thermally activated charge carrier and  $k_B$  is the Boltzmann constant [22]. The field dependent activation energy of  $\text{WSi}_2$  reveals a value of  $\sim 14.6 \text{ meV}$  and  $\sim 14.2 \text{ meV}$ , respectively, in 14 T field, for  $J \parallel [100]$  and  $J \parallel [001]$  [Figs. 3(c) and 3(d)] and is strongly field dependent as observed in  $\text{LaSb}$ ,  $\text{ZrSiS}$  compounds [13,30].

To further investigate the exotic magnetotransport behavior of  $\text{WSi}_2$  single crystal along two principal crystallographic directions, we have performed the Hall resistivity measurements at various temperatures; the data at 2 K is shown in Fig. 4. It is worth mentioning that the field dependence

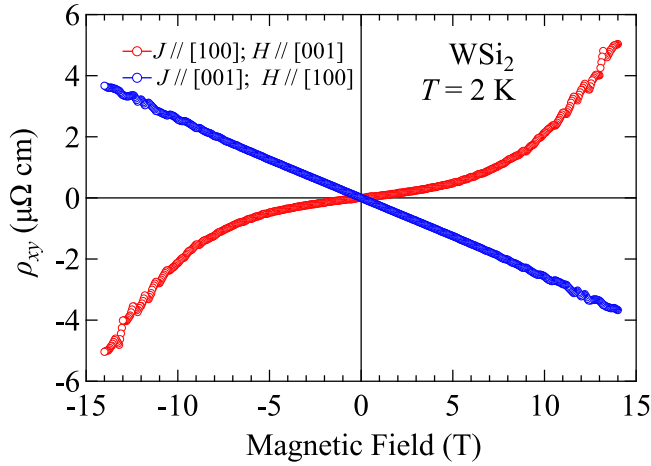


FIG. 4. Hall resistivity ( $\rho_{xy}$ ), measured at  $T = 2$  K, as a function of applied magnetic field for current along the two principal crystallographic directions.

of Hall resistivity data reveals an anisotropic Hall effect depending on the applied field direction. Hall resistivity of  $\text{WSi}_2$  exhibits only positive values for magnetic fields up to 14 T when  $J \parallel [100]$  and  $H \parallel [001]$ . On the other hand, the Hall resistivity is negative for  $J \parallel [001]$  and  $H \parallel [100]$ . The negative (positive) value of Hall resistivity suggests the dominant transporting charge carrier to be electron (hole). The presence of such anisotropic Hall coefficient is thus very interesting and warrants further investigation of the transport phenomena. The occurrence of such anisotropic Hall coefficient has been observed in the single crystals of  $\text{MgB}_2$  in the normal conducting state and in  $\text{EuAl}_4$  [32,33]. The presence of multiple Fermi pockets arising from the multiple bands and their associated charge carrier with transport mobility are solely responsible for such anisotropic Hall resistivity behavior [34]. This type of anisotropy in the Hall effect has recently

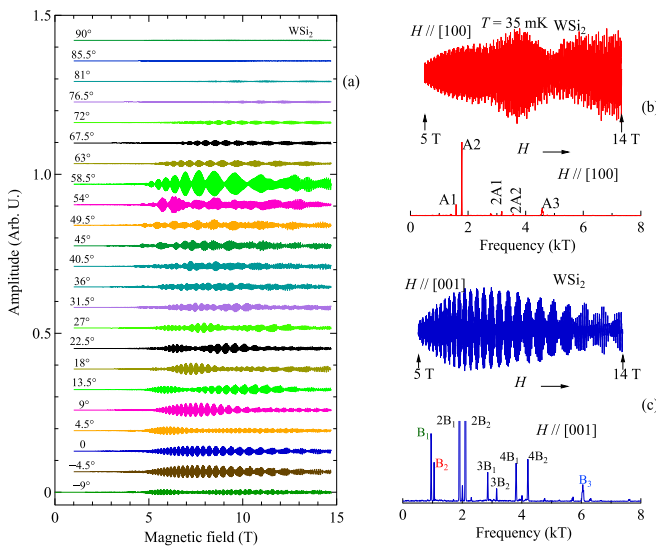


FIG. 5. (a) dHvA quantum oscillations at different field directions from [001] direction to [100] measured at 35 mK, (b) dHvA oscillation and corresponding FFT spectrum for  $H \parallel [100]$ , and (c)  $H \parallel [001]$  at 35 mK.

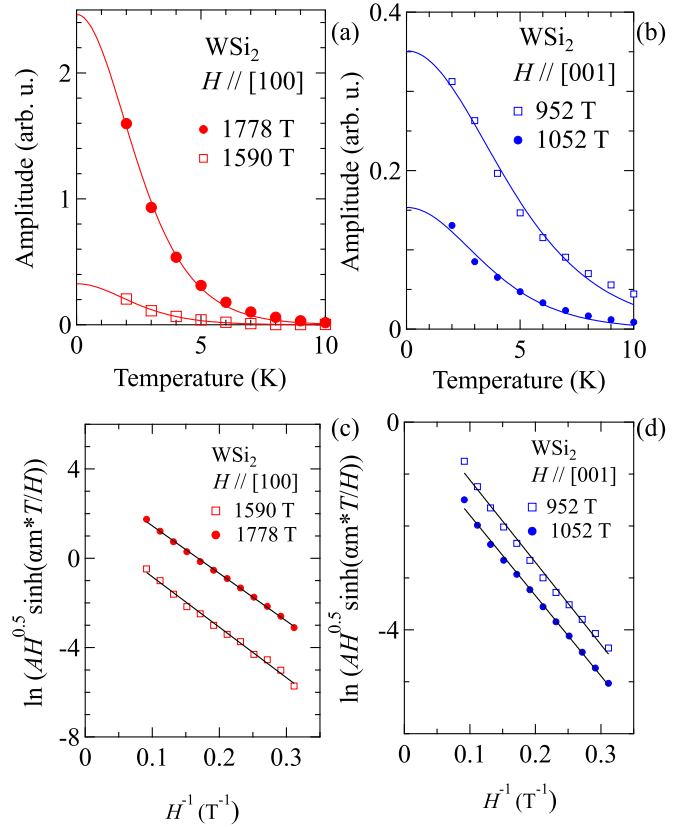


FIG. 6. (a),(b) Temperature dependence of dHvA amplitude and mass plots for the frequencies mentioned along the two principal crystallographic directions (solid lines are the fits, refer to text). (c),(d) Dingle plots along the two principal crystallographic directions of  $\text{WSi}_2$  (solid lines are the fits, refer to text).

been observed in single-crystalline samples of  $\text{NaN}_2\text{As}_2$  and has been termed as goniopolar effect by He *et al.* [35] for single-band systems. They attribute this type of anisotropic Hall effect due to the Fermi surface that has an open concave single band and depending on the applied field direction the charge carriers behave as electrons and holes. However,  $\text{WSi}_2$  is a multiband system and hence the observed anisotropy in the Hall effect can be explained based on the semiclassical multiband transport model of charge carriers as discussed later. In order to envisage the multiband nature and to obtain the number and nature of Fermi pockets present in  $\text{WSi}_2$ , we have performed the band structure calculations and the de Haas-van Alphen quantum oscillation measurements in  $\text{WSi}_2$  which are discussed in the following sections.

### C. de Haas-van Alphen quantum oscillations studies

The temperature and field dependence of magnetization of  $\text{WSi}_2$  revealed robust signature of quantum oscillations when magnetic field was swept along the two principal crystallographic directions. The dHvA quantum oscillations measured at 35 mK at different field directions is shown in Fig. 5(a). The oscillation frequencies are determined by performing a fast Fourier transformation (FFT) of the quantum oscillations [Figs. 5(b) and 5(c)]. The frequencies of oscillations of  $\text{WSi}_2$  obtained from the FFT for  $H \parallel [100]$  are  $A_1 = 1590$  T,  $A_2 =$

TABLE I. Parameters obtained from quantum oscillation analysis  $m^*$ , effective mass;  $T_D$ , Dingle temperature;  $A$ , Fermi surface cross section area,  $k_F$ , Fermi vector;  $v_F$ , Fermi velocity;  $\tau$ , quantum relaxation time,  $l$ , mean free path;  $\mu_q$ , quantum mobility.

	Frequency (T)	$m^*$ ( $m_e$ )	$T_D$ (K)	$A$ ( $\text{nm}^{-2}$ )	$k_F$ ( $10^7 \text{ cm}^{-1}$ )	$v_F$ ( $10^8 \text{ cm/s}$ )	$\tau$ ( $10^{-13} \text{ s}$ )	$l$ (nm)	$\mu_q$ ( $\text{cm}^2/\text{Vs}$ )
$H \parallel [100]$	1590	0.212	7.25	15.22	2.20	1.202	1.679	201.9	1390
	1778	0.204	7.11	17.02	2.32	1.322	1.712	226.4	1470
	4573								
$H \parallel [001]$	952	0.111	9.70	91.13	1.70	1.777	1.255	223.1	1990
	1052	0.141	7.47	10.07	1.79	1.471	1.629	239.7	2030
	6045								

1778 T, and  $A_3 = 4573 \text{ T}$  in which  $A_1$  and  $A_2$  are for electron pockets and  $A_3$  is for hole pocket. Subsequently, the obtained frequencies for  $H \parallel [001]$  are  $B_1 = 952 \text{ T}$ ,  $B_2 = 1052 \text{ T}$ , and  $B_3 = 6045 \text{ T}$  in which  $B_1$  and  $B_2$  are for hole pockets and  $B_3$  is for electron pocket. It is to be mentioned here that some other observed peaks in the FFT spectrum can be explained as the higher harmonics of the fundamental frequencies and as a combination of fundamental frequencies ( $mA_1 \pm nA_2$ ), the origin of which could be attributed to the different magnetic interactions [36]. The temperature variation of FFT amplitude of dHvA oscillations of  $\text{WSi}_2$  is shown in Fig. 6 and is fitted to the thermal damping factor of Lifshitz-Kosevich formula:  $R_T = (X/\sinh X)$ , where  $X = (\lambda T m^*/H)$ ,  $\lambda = (2\pi^2 k_B m_e / e \hbar)$  which is a constant equal to a value 14.69 T and  $m^*$  corresponds to the cyclotron effective mass of charge carriers in the unit of free electron mass  $m_e$  [15,22,36]. The magnetic field induced damping of the quantum oscillation amplitude data of  $\text{WSi}_2$  have been fitted to the equation:  $R_B = \exp(-\lambda T_D m^*/H)$  to determine the Dingle temperature  $T_D$  at 2 K and hence to calculate the quantum mobility  $\mu_Q = (e/2\pi k_B T_D m^*)$  for the different bands. The carrier effective masses and other quantum parameters corresponding to the different frequencies have been extracted and are given in Table I.

From the compilation of angular dependence of all the fundamental frequencies obtained from the FFT spectrum of dHvA oscillations, the information about the Fermi surface is obtained and is shown in Fig. 7(a). A comparison of the Fermi surface obtained from the theoretical LDA calculation of  $\text{WSi}_2$  is also shown in Fig. 7(b). A part of the Fermi surface of  $\text{WSi}_2$  formed by frequencies  $B_1$  and  $B_2$  which belongs to the two branches as shown in Fig. 7(a) follows a  $(\cos\theta)^{-1}$  behavior up to  $\theta \approx 55^\circ$  thereby indicating a cylindrical Fermi surface of  $\text{WSi}_2$  [26,37]. If one compares the angular dependence of the dHvA frequencies and the corresponding LDA calculations of  $\text{WSi}_2$  as shown in Fig. 7, a dumbbell shaped hole pockets at around the  $\Gamma$  point arise wherein the orbits  $B_1$  and  $B_2$  correspond to the minimum and maximum cross-sectional areas following the Onsager relation for Fermi surface where the frequency of oscillations is directly proportional to the extremal cross-sectional area ( $A$ ) of the Fermi surface:  $F = (\hbar A / 2\pi e)$ , where  $\hbar$  represents the reduced Planck constant and  $e$  is the electronic charge [22,38–40]. The electronic band structure calculations of  $\text{WSi}_2$  suggests the electron-type and hole-type bands are centered at the high symmetric Z point and  $\Gamma$  point, respectively. While the hole-type bands form the dumbbell shaped cylindrical Fermi

surface, the electron-type bands form the four-cornered rosette shaped Fermi surface.

The calculated dHvA frequencies based on the density functional theory using LDA approximation reveals three distinct frequencies at 1430 T, 1583 T, and 4356 T for  $H \parallel [100]$  with band masses  $0.445m_e$ ,  $0.451m_e$ , and  $0.783m_e$  and 809 T, 894 T, and 5901 T for  $H \parallel [001]$  with band masses  $0.217m_e$ ,  $0.249m_e$ , and  $1.306m_e$  for  $H \parallel [100]$ . The calculated band masses are slightly heavier than the experimental results. This discrepancy may be attributed to the shortcomings of the LDA for semimetals. In the band structure calculations, the self-consistent one electron wave function is a

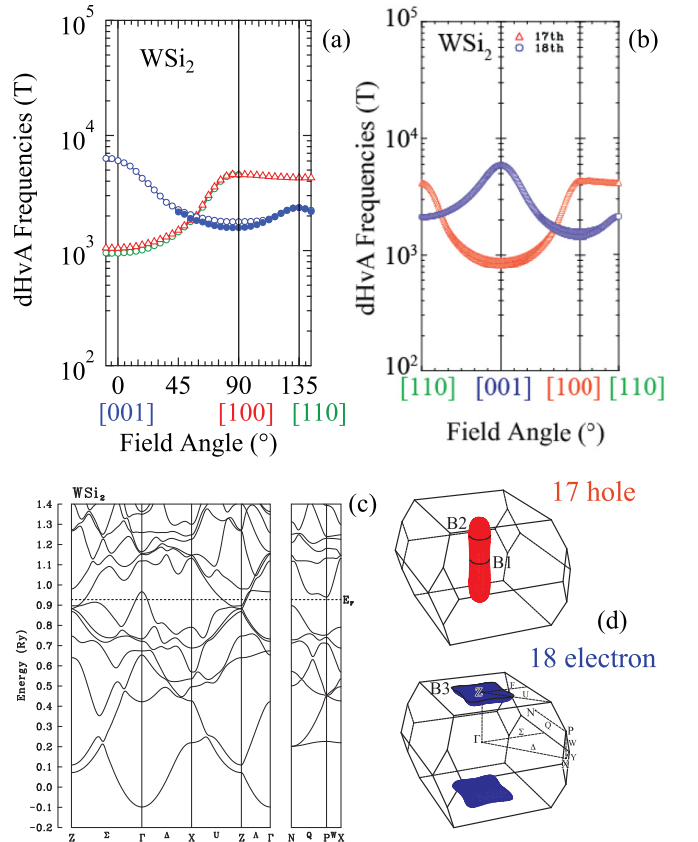


FIG. 7. (a) Angular dependence of the dHvA frequency from [001] to [100] to [110] direction, (b) the corresponding theoretical calculation, (c) the band structure calculations, and (d) the corresponding hole and electron Fermi surfaces.

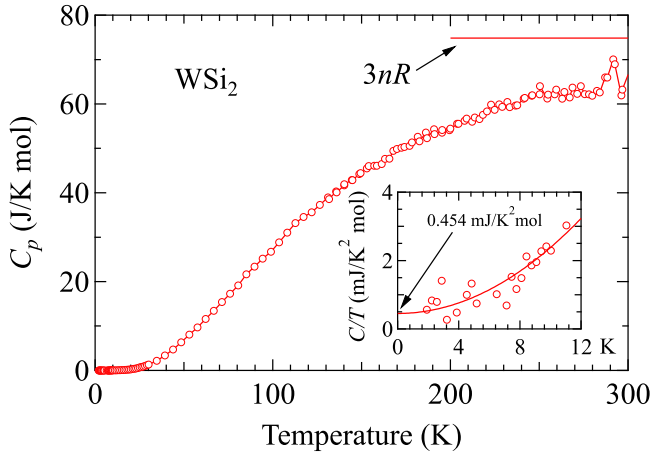


FIG. 8. Heat capacity of  $\text{WSi}_2$ . The inset shows the low temperature part in the form of  $C/T$  vs  $T$ .

combination of the kinetic energy, the external potential, and the classical Coulomb potential, which includes self-interaction. The last term represents exchange-correlation potential which is typically a complicated functional of the local charge density  $\rho(\mathbf{r})$ , and its exact form is unknown [41]. The theoretical Sommerfeld coefficient  $\gamma_b$  and the corresponding density of states at the Fermi level were calculated to be  $0.473 \text{ mJ/K}^2 \text{ mol}$  and  $2.733 \text{ states/Ry}$ . In order to estimate the experimental Sommerfeld coefficient we measured the heat capacity of  $\text{WSi}_2$  in the temperature 2–300 K as shown in Fig. 8. The heat capacity did not show any anomaly in the measured temperature range and attains a value of about  $63 \text{ J/K mol}$ , which is close to the Dulong and Petit limiting value of  $3nR (= 74.84 \text{ J/K mol})$ . The inset of Fig. 8 shows the low temperature plot of  $C/T$  vs  $T$ . The solid line is fit to the expression  $C/T = \gamma + \beta T^2$  where  $\gamma T$  is the electronic contribution and  $\beta T^3$  is the phononic contribution. The gamma value thus estimated is  $0.454 \text{ mJ/K}^2 \text{ mol}$  and  $\beta$  value is  $0.019 \text{ mJ/K}^4 \text{ mol}$ . The experimentally observed  $\gamma$  value matches well with the band structure calculation. Furthermore, we estimated the density of states at the Fermi level from the expression:  $\mathcal{D}_\gamma(E_F) = \frac{3\gamma}{\pi^2 k_B}$ , substituting the experimental value of  $\gamma$  in the above equation, we get the density of states as  $0.192 \text{ states/eV f.u.}$ , which when converted to units of Rydberg, we obtain  $\mathcal{D}_\gamma(E_F) = 2.62 \text{ states/Ry}$  which matches well with the theoretical estimation as mentioned above.

To investigate the topological semimetallic signature (if any) in  $\text{WSi}_2$ , we have analyzed the field and temperature dependence of the dHvA data in the framework of Lifshitz-Kosevich formalism in which the field dependence of magnetization can be expressed as:

$$\Delta M = \sum_{i=\alpha,\beta} A_i H^{1/2} R_T^i R_D^i R_S^i \sin \left[ 2\pi \left( \frac{F_i}{H} - \gamma + \delta \right) \right], \quad (1)$$

where,  $R_T$ ,  $R_D$ , and  $R_S$  are components representing the damping of oscillations due to the temperature, magnetic field, and spin, respectively [22,36]. The  $\gamma$  in Eq. (1) assumes a value 0 for a linear band and  $1/2$  for parabolic band. The phase shift in Eq. (1), represented by  $\delta$  is estimated from the dimensionality

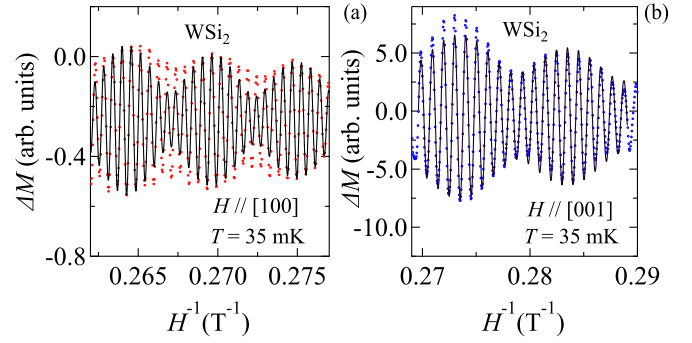


FIG. 9. (a),(b) LK formula fitting to the magnetic quantum oscillation data measured at 35 mK along the two principal crystallographic directions.

of the Fermi surface. The phase shift  $\delta$  assumes a value 0 and  $\pm 1/8$  for two-dimensional (2D) and three-dimensional (3D) Fermi surface, respectively. The positive and negative values of  $\delta$  are for the minimum and maximum cross-sectional areas in 3D Fermi surface, respectively. The total phase of the magnetic oscillations in the above Eq. (1) is  $\psi = (-\gamma + \delta)$ . In case of parabolic band,  $\gamma = (1/2 - \phi_B/2\pi)$  where  $\phi_B$  represents the Berry phase. The Berry phase is accounted for an additional geometrical phase acquired along a closed trajectory in the parameter space during an adiabatic evolution [38–40,42]. For a material with topologically trivial 3D band, one would expect  $\phi_B$  to be 0, hence the total phase  $\psi$  assumes a value  $(-1/2 \pm 1/8) = -3/8$  or  $-5/8$  for minimum and maximum cross-sectional areas, respectively. On the other hand, for a topologically nontrivial 3D band,  $\phi_B = \pi$ , hence one would expect the total phase  $\psi$  to be equal to  $+1/8$  and  $-1/8$  for minimum and maximum cross-sectional areas, respectively. It is to be noted that the value of  $\psi$  is affected by the sign of the spin damping factor  $R_S$  [38–40]. We have fitted the magnetic oscillations data of  $\text{WSi}_2$  to the Lifshitz-Kosevich (LK) formula in order to extract the Berry phase as shown in Fig. 9. From the fit to the LK formula, the total phase,  $\psi$  for  $\text{WSi}_2$  assumes value  $\sim -0.125$  and  $+0.006$ , respectively, for  $B_1 = 952 \text{ T}$  and  $B_2 = 1052 \text{ T}$  when  $H \parallel [001]$ . Similarly when  $H \parallel [100]$ , the same phase takes the value  $\sim +0.070$  and  $-0.130$  for  $A_1 = 1590 \text{ T}$ ,  $A_2 = 1778 \text{ T}$ , respectively. The obtained values of the total phase factors for different frequency branches thereby indicate the Berry phase corresponding to the topologically nontrivial features that is present in  $\text{WSi}_2$ .

More precise and accurate value of the Berry phase can also be estimated from the Landau level (LL) fan diagram as described in Fig. S1 in the Supplemental Material [43]. Although the LK analysis of the dHvA oscillations gives some hint about the nontrivial Berry phase, the electronic band structure calculation does not provide any evidence of linear band inversion having distinct Dirac/Weyl nodes. Hence the electronic structure of  $\text{WSi}_2$  is not in line with the experimentally observed nontrivial features, such as metal to semiconductor and XMR behavior in applied magnetic fields, as observed in other topological systems. The observed nontrivial features in  $\text{WSi}_2$  may also originate from the spin texture which was evident in the sister compound  $\text{MoSi}_2$  [26].

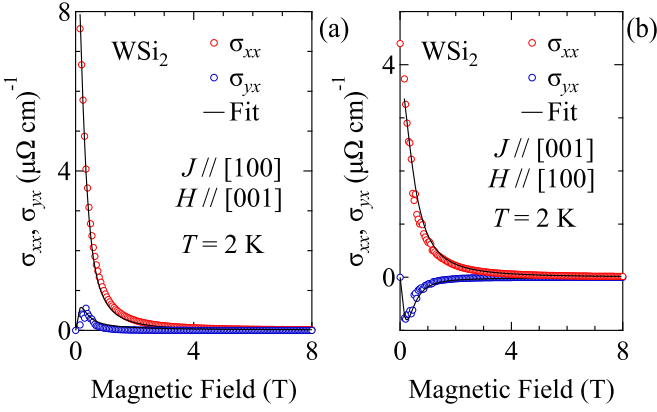


FIG. 10. Longitudinal and Hall conductivity as a function of magnetic field of  $\text{WSi}_2$  at  $T = 2$  K, the solid lines depict the fit to the multiband model (refer to text).

The  $d$  orbitals of heavy atoms like Mo, W may attribute to the strong spin-orbit coupling leading to such spin texture which in turn gives rise to such topological features as observed in other topological systems [13].

#### D. Multiband model: Magnetotransport data

From the analyses of dHvA quantum oscillations data and the electronic band structure calculations of  $\text{WSi}_2$ , the presence of multibands and the multiple Fermi pockets has been evidenced. Hence, we analyzed the magnetotransport data based on a multiband transport model [13,30,44,45]. We have estimated the charge carrier density and carrier mobility from the field dependence of transverse linear resistivity ( $\rho_{xx}$ ) and Hall resistivity ( $\rho_{xy}$ ) using the multiband transport model. According to the semiclassical Drude model, the conductivities of individual Fermi pockets (either electron or hole pockets) are summed up to get the total conductivity of the longitudinal and transverse counterpart of the conductivity tensor as given in the following expressions:

$$\sigma_{xx} = \sum_{i=1,2,3..} \left( \frac{en_i\mu_i}{1 + (\mu_i H)^2} \right) \quad (2)$$

$$\sigma_{xy} = -\sigma_{yx} = \sum_{i=1,2,3..} \left( \frac{en_i\mu_i^2 H}{1 + (\mu_i H)^2} \right), \quad (3)$$

where the index  $i$  stands for the contributions from different Fermi pockets.  $n_i$  is the charge carrier concentration and  $\mu_i$  represents the carrier transport mobility for the corresponding charge carriers. The component of conductivity tensor can be deduced from the transverse magnetoresistivity ( $\rho_{xx}$ ) and Hall resistivity ( $\rho_{xy}$ ) data with the help of tensorial inversion of the total resistivity matrix as follows [31,45]:

$$\sigma_{xx} = \rho_{xx}/(\rho_{xx}^2 + \rho_{xy}^2) \quad (4)$$

$$\sigma_{yx} = \rho_{xy}/(\rho_{xx}^2 + \rho_{xy}^2). \quad (5)$$

The plots of field variation of magnetoconductivity of  $\text{WSi}_2$  along the two principal crystallographic directions are shown in Fig. 10, calculated as per Eqs. (4) and (5). There is a large anisotropy in the Hall conductivity data. In order to de-

termine the transport carrier densities and the corresponding carrier mobilities, we have fitted the field variation of linear magnetoconductivity ( $\sigma_{xx}$ ) and the Hall conductivity ( $\sigma_{yx}$ ) data to the above expressions Eqs. (2) and (3), respectively. It is to be noted here that in  $\text{WSi}_2$ , there exists two electron pockets and one hole pocket when field is applied along the [100] direction. On the other hand, there are two hole pockets and one electron pocket when field is applied along [001] direction as has been evidenced from the dHvA analyses of  $\text{WSi}_2$ . In line with the dHvA analyses, we have considered a similar number of Fermi pockets (electrons and holes) while fitting the magnetoconductivity data. Hence, the magnetoconductivity based on Eq. (3) for  $H \parallel [001]$  and [100] can be written as:

$$\sigma_{yx}^{[001]} = \frac{en_{h1}\mu_{h1}^2 H}{1 + (\mu_{h1}H)^2} + \frac{en_{h2}\mu_{h2}^2 H}{1 + (\mu_{h2}H)^2} - \frac{en_{e1}\mu_{e1}^2 H}{1 + (\mu_{e1}H)^2} \quad (6)$$

and

$$\sigma_{yx}^{[100]} = \frac{en_{h1}\mu_{h1}^2 H}{1 + (\mu_{h1}H)^2} - \frac{en_{e1}\mu_{e1}^2 H}{1 + (\mu_{e1}H)^2} - \frac{en_{e2}\mu_{e2}^2 H}{1 + (\mu_{e2}H)^2}. \quad (7)$$

The obtained fitting parameters are listed in Table II. From these extracted fitting parameters it is obvious that for  $J \parallel [100]$  and  $H \parallel [001]$  as per Eq. (6), the total hole contribution is larger than total electron contribution so that  $\sigma_{yx} > 0$  or  $\rho_{xy} > 0$  in the field range 0 to 14 T. On the other hand for  $J \parallel [001]$  and  $H \parallel [100]$  as per Eq. (7) the total electron contribution is larger than the total hole contribution so that  $\sigma_{yx} < 0$  or  $\rho_{xy} < 0$  in the field range 0 to 14 T thus explaining the observed anisotropy in the Hall effect. It is to be mentioned here that an anisotropic Hall effect was also observed in the isostructural  $\text{MoSi}_2$  compound, however only up to 0.25 T at  $T = 2$  K while for higher magnetic fields an electron dominated transport phenomena was observed along both directions unlike in the present case [26].

From the analysis of Hall effect of  $\text{WSi}_2$ , it is clear that there is nearly a compensation of the charge carriers in  $\text{WSi}_2$  and the mobility also assumes a very large value and is comparable to that of the recently reported topological semimetals [4,7,11–14,16–18,21–23,26,31,44]. The value of carrier density in  $\text{WSi}_2$  is well within the similar order as expected for a semimetal, thereby ascribing  $\text{WSi}_2$  to be a semimetal. The extremely large magnetoresistance accompanied by the ultra-large transport carrier mobility is reminiscent for a topological semimetal. The origin of such an ultra-large carrier mobility in  $\text{WSi}_2$  could be due to the strong suppression of backward scattering which is quite often observed in topological semimetals. The indirect way to elucidate the suppression of backscattering is often reported in the literature as the ratio ( $r$ ) of classical transport lifetime ( $\tau_{tr}$ ) of scattering to the quantum lifetime ( $\tau_Q$ ) of the scattering. The  $\tau_{tr}$  is determined from the carrier transport mobility ( $\mu_{tr}$ ) which is obtained from the Hall conductivity data by using the relationship:  $\tau_{tr} = (\mu_{tr} m^*)/e$ . Similarly,  $\tau_Q$  is obtained from the quantum mobility ( $\mu_Q$ ), estimated from the quantum oscillations data [18]. The ratio,  $r$  estimated from the ratio of quantum mobility to the classical transport mobility reads a value of only a few tens ( $\approx 30$ ) for different Fermi pockets, suggesting a weak topological protection.

TABLE II. Carrier concentration and mobility extracted from the multiband model fit of the  $\sigma_{xx}$  and  $\sigma_{xy}$  data.

$\rho_{xy}$	$n_{h1}$ ( $10^{20} \text{ cm}^{-3}$ )	$n_{h2}$ ( $10^{20} \text{ cm}^{-3}$ )	$n_{e1}$ ( $10^{20} \text{ cm}^{-3}$ )	$n_{e2}$ ( $10^{20} \text{ cm}^{-3}$ )	$\mu_{h1}$ ( $10^4 \text{ cm}^2/\text{V s}$ )	$\mu_{h2}$ ( $10^4 \text{ cm}^2/\text{V s}$ )	$\mu_{e1}$ ( $10^4 \text{ cm}^2/\text{V s}$ )	$\mu_{e2}$ ( $10^4 \text{ cm}^2/\text{V s}$ )
$J \parallel [001]$	6.19	...	5.72	0.91	1.85	...	3.1	2.1
$H \parallel [100]$								
$J \parallel [100]$	7.52	1.86	8.46	...	3.9	3.25	3.4	...
$H \parallel [001]$								

Usually, the observation of XMR can be understood from the topological protection mechanism, which necessitates a nontrivial topological state that suppresses the backscattering mechanism. The band structure analysis along with ARPES studies of electronic structure are the direct ways of envisaging the nontrivial topological states. Since no such evidence of nontrivial topological states like band inversion or linear dispersion in the bulk bands, or Weyl nodes are observed from our band structure calculations, although the magnetotransport properties are reminiscent of other topological material systems, the novel topological protection mechanism may not be the reason for the observed XMR in  $\text{WSi}_2$ . However, the perfect carrier compensation along with large carrier mobility are the reasons for the observed XMR in  $\text{WSi}_2$ .

#### IV. SUMMARY AND CONCLUSIONS

A detailed anisotropic magnetotransport and Fermi surface studies have been performed on a high quality single-crystalline  $\text{WSi}_2$  sample grown by Czochralski method in a tetra-arc furnace. Three main fundamental frequencies were observed from our dHvA studies and all these three frequencies were also determined from the band structure calculations. The angular dependence of the dHvA frequencies agrees well with the calculations. The magnetoresistance shows an unprecedentedly large value of  $10^5\%$  without showing any sign of saturation in a field of 14 T at 2 K. The anisotropic Hall coefficient in  $\text{WSi}_2$  ascertains the presence

of multiple Fermi pockets from multiple bands having low carrier densities and very large transport mobilities. The near compensation of charge carriers and the large carrier mobility in  $\text{WSi}_2$  are solely responsible for such a XMR behavior. The observed features like large RRR, low carrier density, near compensation of charge carriers, high transport mobility, and suppression of backward scattering revealed that this compound is a compensated semimetal hosting XMR behavior which is reminiscent to other topological semimetals. A nontrivial Berry phase was revealed from the dHvA quantum oscillation studies. Further experiments like angle resolved photo emission spectroscopy and a detailed band structure analysis will shed more light on the topological features of  $\text{WSi}_2$  single crystal, if any.

#### ACKNOWLEDGMENTS

The author R.M. thanks Tata Institute of Fundamental Research, Mumbai, for the post-doctoral fellowship. The authors R.M. and A.T. thank J-Physics:Physics of Conductive Multipole Systems for the travel assistance for performing dHvA experiments at IMR, Tohoku University, Japan. D.A. and H.H. acknowledge the financial support by KAKENHI (JP15H05882, JP15H05884, JP15H05886, JP15K21732, JP18F18017, JP19H00646), and GIMRT (19F0501). International Research Center for Nuclear Materials Science, Institute for Materials Research, Tohoku University is gratefully acknowledged for assistance through a collaborative research.

- 
- [1] M. Z. Hasan and C. L. Kane, *Rev. Mod. Phys.* **82**, 3045 (2010).  
[2] T. Liang, Q. Gibson, M. N. Ali, M. Liu, R. J. Cava, and N. P. Ong, *Nat. Mater.* **14**, 280 (2015).  
[3] S.-Y. Xu, I. Belopolski, N. Alidoust, M. Neupane, G. Bian, C. Zhang, R. Sankar, G. Chang, Z. Yuan, C.-C. Lee *et al.*, *Science* **349**, 613 (2015).  
[4] H. Weng, C. Fang, Z. Fang, B. A. Bernevig, and X. Dai, *Phys. Rev. X* **5**, 011029 (2015).  
[5] S. Jia, S.-Y. Xu, and M. Z. Hasan, *Nat. Mater.* **15**, 1140 (2016).  
[6] N. P. Armitage, E. J. Mele, and A. Vishwanath, *Rev. Mod. Phys.* **90**, 015001 (2018).  
[7] M. N. Ali, J. Xiong, S. Flynn, J. Tao, Q. D. Gibson, L. M. Schoop, T. Liang, N. Haldolaarachchige, M. Hirschberger, N. P. Ong *et al.*, *Nature (London)* **514**, 205 (2014).  
[8] A. A. Soluyanov, D. Gresch, Z. Wang, Q. Wu, M. Troyer, X. Dai, and B. A. Bernevig, *Nature (London)* **527**, 495 (2015).  
[9] M.-Y. Yao, N. Xu, Q. S. Wu, G. Autès, N. Kumar, V. N. Strocov, N. C. Plumb, M. Radovic, O. V. Yazyev, C. Felser, J. Mesot, and M. Shi, *Phys. Rev. Lett.* **122**, 176402 (2019).  
[10] X.-C. Pan, X. Wang, F. Song, and B. Wang, *Adv. in Phys.: X* **3**, 1468279 (2018).  
[11] J. He, C. Zhang, N. J. Ghimire, T. Liang, C. Jia, J. Jiang, S. Tang, S. Chen, Y. He, S.-K. Mo *et al.*, *Phys. Rev. Lett.* **117**, 267201 (2016).  
[12] C. Shekhar, A. K. Nayak, Y. Sun, M. Schmidt, M. Nicklas, I. Leermakers, U. Zeitler, Y. Skourski, J. Wosnitza, Z. Liu *et al.*, *Nat. Phys.* **11**, 645 (2015).  
[13] F. Tafti, Q. Gibson, S. Kushwaha, N. Haldolaarachchige, and R. J. Cava, *Nat. Phys.* **12**, 272 (2016).  
[14] N. J. Ghimire, Y. Luo, M. Neupane, D. Williams, E. Bauer, and F. Ronning, *J. Phys.: Condens. Matter* **27**, 152201 (2015).

- [15] J. Hu, J. Liu, D. Graf, S. Radmanesh, D. Adams, A. Chuang, Y. Wang, I. Chiorescu, J. Wei, L. Spinu *et al.*, *Sci. Rep.* **6**, 18674 (2016).
- [16] C. Zhang, C. Guo, H. Lu, X. Zhang, Z. Yuan, Z. Lin, J. Wang, and S. Jia, *Phys. Rev. B* **92**, 041203(R) (2015).
- [17] F. C. Chen, H. Y. Lv, X. Luo, W. J. Lu, Q. L. Pei, G. T. Lin, Y. Y. Han, X. B. Zhu, W. H. Song, and Y. P. Sun, *Phys. Rev. B* **94**, 235154 (2016).
- [18] N. Kumar, Y. Sun, N. Xu, K. Manna, M. Yao, V. Süss, I. Leermakers, O. Young, T. Förster, M. Schmidt *et al.*, *Nat. Commun.* **8**, 1642 (2017).
- [19] M. N. Ali, L. M. Schoop, C. Garg, J. M. Lippmann, E. Lara, B. Lotsch, and S. S. Parkin, *Sci. Adv.* **2**, e1601742 (2016).
- [20] P. Kapitza, *Proc. R. Soc. Lond. A. Mathematical and Physical Sciences* **119**, 358 (1928).
- [21] N. Ghimire, A. Botana, D. Phelan, H. Zheng, and J. F. Mitchell, *J. Phys.: Condens. Mat.* **28**, 235601 (2016).
- [22] F. F. Tafti, Q. Gibson, S. Kushwaha, J. W. Krizan, N. Haldolaarachchige, and R. J. Cava, *Proc. Nat. Acad. Sci.* **113**, E3475 (2016).
- [23] J. Nayak, S.-C. Wu, N. Kumar, C. Shekhar, S. Singh, J. Fink, E. E. Rienks, G. H. Fecher, S. S. Parkin, B. Yan *et al.*, *Nat. Commun.* **8**, 13942 (2017).
- [24] X. Huang, L. Zhao, Y. Long, P. Wang, D. Chen, Z. Yang, H. Liang, M. Xue, H. Weng, Z. Fang *et al.*, *Phys. Rev. X* **5**, 031023 (2015).
- [25] L. Šmejkal, Y. Mokrousov, B. Yan, and A. H. MacDonald, *Nat. Phys.* **14**, 242 (2018).
- [26] M. Matin, R. Mondal, N. Barman, A. Thamizhavel, and S. K. Dhar, *Phys. Rev. B* **97**, 205130 (2018).
- [27] O. Laborde, O. Thomas, J. Senateur, and R. Madar, *J. Phys. F: Met. Phys.* **16**, 1745 (1986).
- [28] F. Nava, E. Mazzega, M. Michelini, O. Laborde, O. Thomas, J. Senateur, and R. Madar, *J. Appl. Phys.* **65**, 1584 (1989).
- [29] M. N. Ali, L. Schoop, J. Xiong, S. Flynn, Q. Gibson, M. Hirschberger, N. P. Ong, and R. J. Cava, *EPL (Europhys. Lett.)* **110**, 67002 (2015).
- [30] R. Singha, A. K. Pariari, B. Satpati, and P. Mandal, *Proc. Natl. Acad. Sci.* **114**, 2468 (2017).
- [31] O. Pavlosiuk, P. Swatek, D. Kaczorowski, and P. Wiśniewski, *Phys. Rev. B* **97**, 235132 (2018).
- [32] Y. Eltsev, K. Nakao, S. Lee, T. Masui, N. Chikumoto, S. Tajima, N. Koshizuka, and M. Murakami, *Phys. Rev. B* **66**, 180504(R) (2002).
- [33] S. Araki, Y. Ikeda, T. C. Kobayashi, A. Nakamura, Y. Hiranaka, M. Hedo, T. Nakama, and Y. Ōnuki, *J. Phys. Soc. Jpn.* **83**, 015001 (2014).
- [34] S. N. Zhang, Q. S. Wu, Y. Liu, and O. V. Yazyev, *Phys. Rev. B* **99**, 035142 (2019).
- [35] B. He, Y. Wang, M. Q. Arguilla, N. D. Cultrara, M. R. Scudder, J. E. Goldberger, W. Windl, and J. P. Heremans, *Nat. Mater.* **18**, 568 (2019).
- [36] D. Shoenberg, *Magnetic Oscillations in Metals* (Cambridge University Press, Cambridge, England, 2009).
- [37] J. M. Van Ruitenbeek, W. Joss, R. Pauthenet, O. Thomas, J. P. Senateur, and R. Madar, *Phys. Rev. B* **35**, 7936 (1987).
- [38] Z. J. Xiang, D. Zhao, Z. Jin, C. Shang, L. K. Ma, G. J. Ye, B. Lei, T. Wu, Z. C. Xia, and X. H. Chen, *Phys. Rev. Lett.* **115**, 226401 (2015).
- [39] C. M. Wang, H.-Z. Lu, and S.-Q. Shen, *Phys. Rev. Lett.* **117**, 077201 (2016).
- [40] K.-W. Chen, X. Lian, Y. Lai, N. Aryal, Y.-C. Chiu, W. Lan, D. Graf, E. Manousakis, R. E. Baumbach, and L. Balicas, *Phys. Rev. Lett.* **120**, 206401 (2018).
- [41] M. Kakihana, K. Nishimura, T. Takeuchi, Y. Haga, H. Harima, M. Hedo, T. Nakama, and Y. Ōnuki, *J. Phys. Soc. Jpn.* **88**, 044712 (2019).
- [42] M. V. Berry, *Proc. Royal Soc. London. A. Mathematical and Physical Sciences* **392**, 45 (1984).
- [43] See Supplemental Material at <http://link.aps.org/supplemental/10.1103/PhysRevB.102.115158> for a Landau level fan diagram.
- [44] O. Pavlosiuk and D. Kaczorowski, *Sci. Rep.* **8**, 11297 (2018).
- [45] J. Xu, N. J. Ghimire, J. S. Jiang, Z. L. Xiao, A. S. Botana, Y. L. Wang, Y. Hao, J. E. Pearson, and W. K. Kwok, *Phys. Rev. B* **96**, 075159 (2017).